

Supplementary material of: Energetically Stringent Quantification of Water Vapor Supersaturation at Cloud Base

Ramon C. Braga¹, Daniel Harrison¹, Manfred Wendisch² and Rachel Albrecht³

¹ Reefs and Oceans Research Cluster, National Marine Science Centre, Southern Cross University, Coffs Harbour, Australia.

² Leipzig Institute for Meteorology, Leipzig University, Leipzig, Germany.

³ Instituto de Astronomia, Geofísica e Ciências Atmosféricas, Universidade de São Paulo, São Paulo, Brazil.

Correspondence to: Ramon C. Braga (ramon.braga@scu.edu.au)

This PDF file includes:

Supplementary Figures to the main text: S1 to S11.

Section S1: Thermodynamic Analysis of the Energetic Budget and Supersaturation at Warm Cloud Base

25

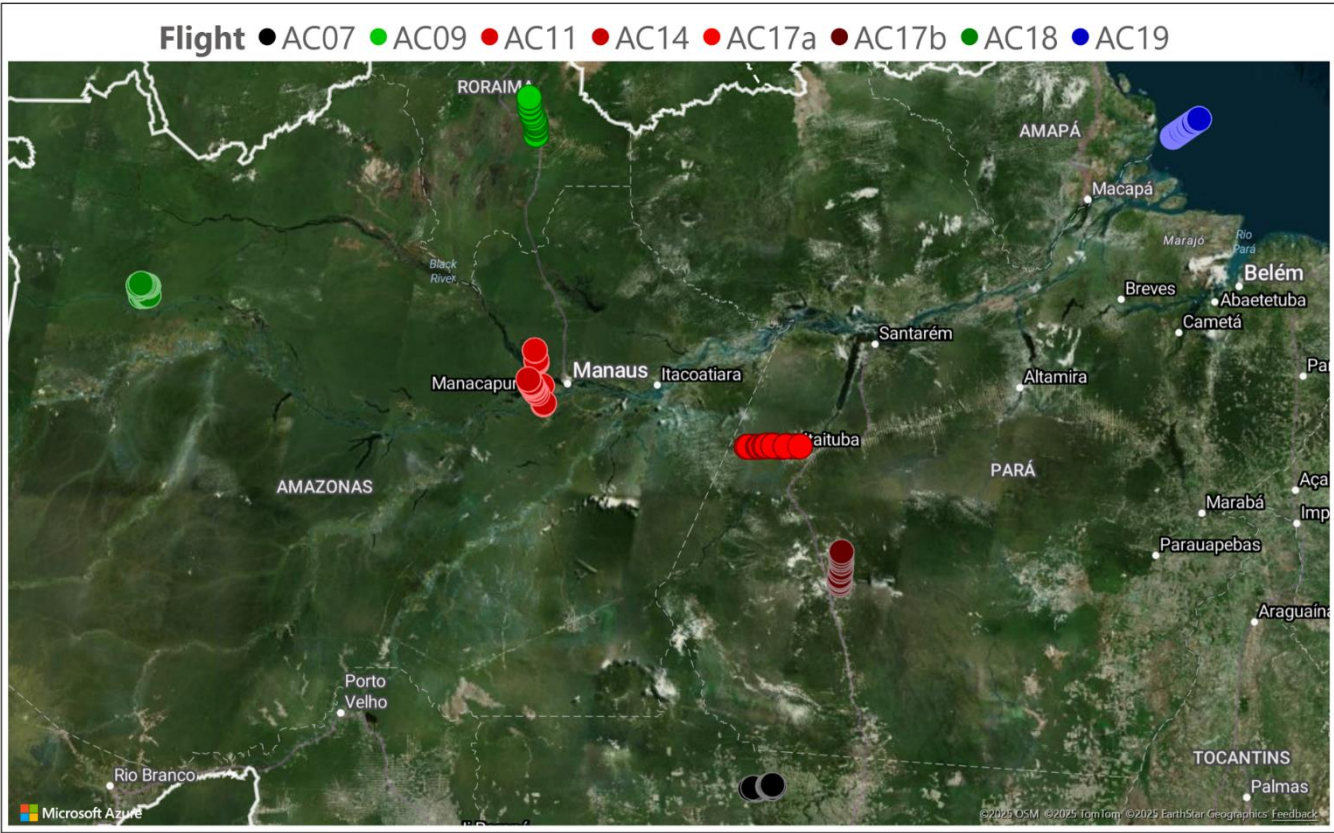


Fig. S1. Regions of measurements at cloud bases of cumulus clouds during the ACRIDICON-CHUVA campaign. Flights are color-coded and labelled at the top.

30

Flight AC07: Deforestation Arc

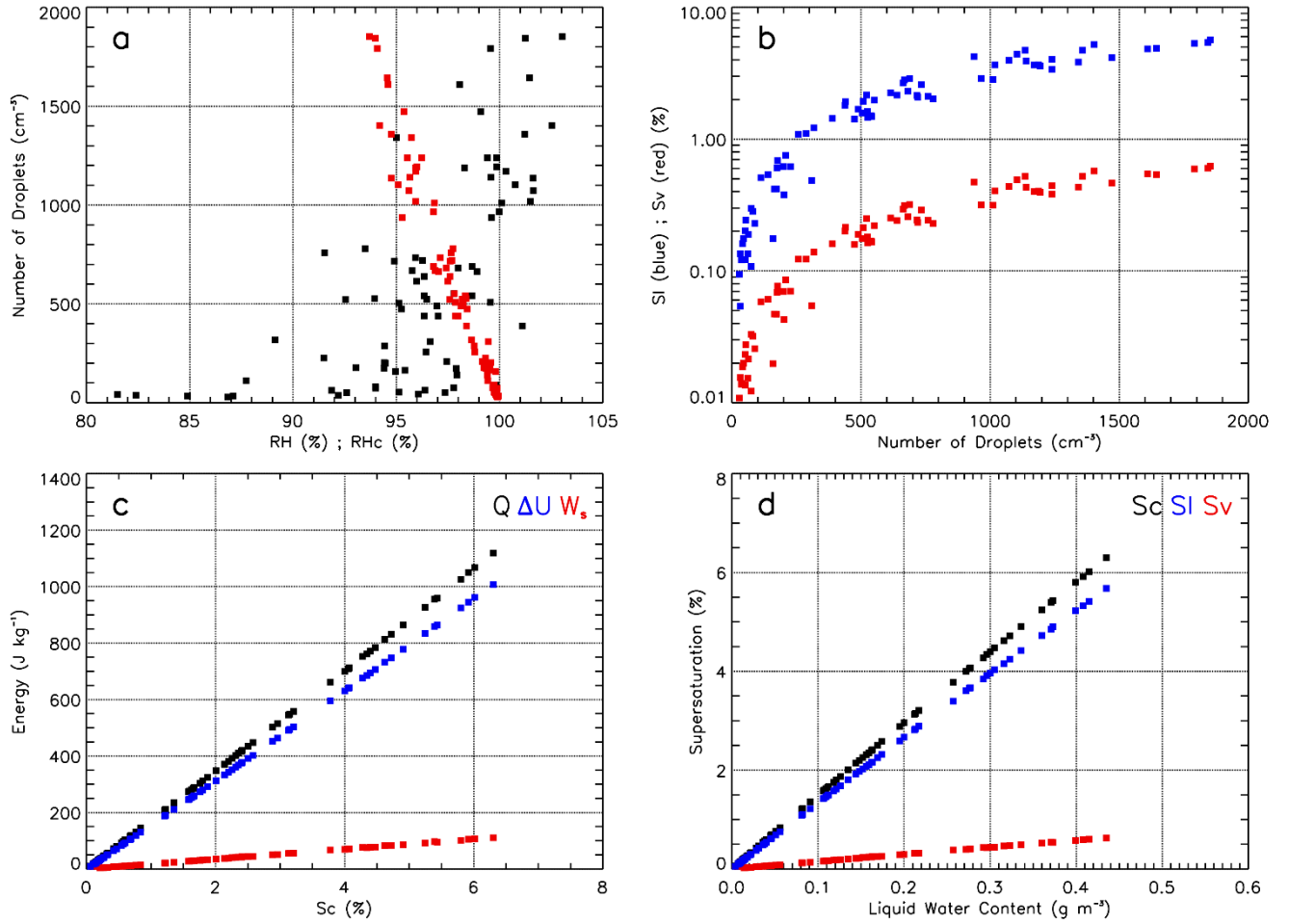
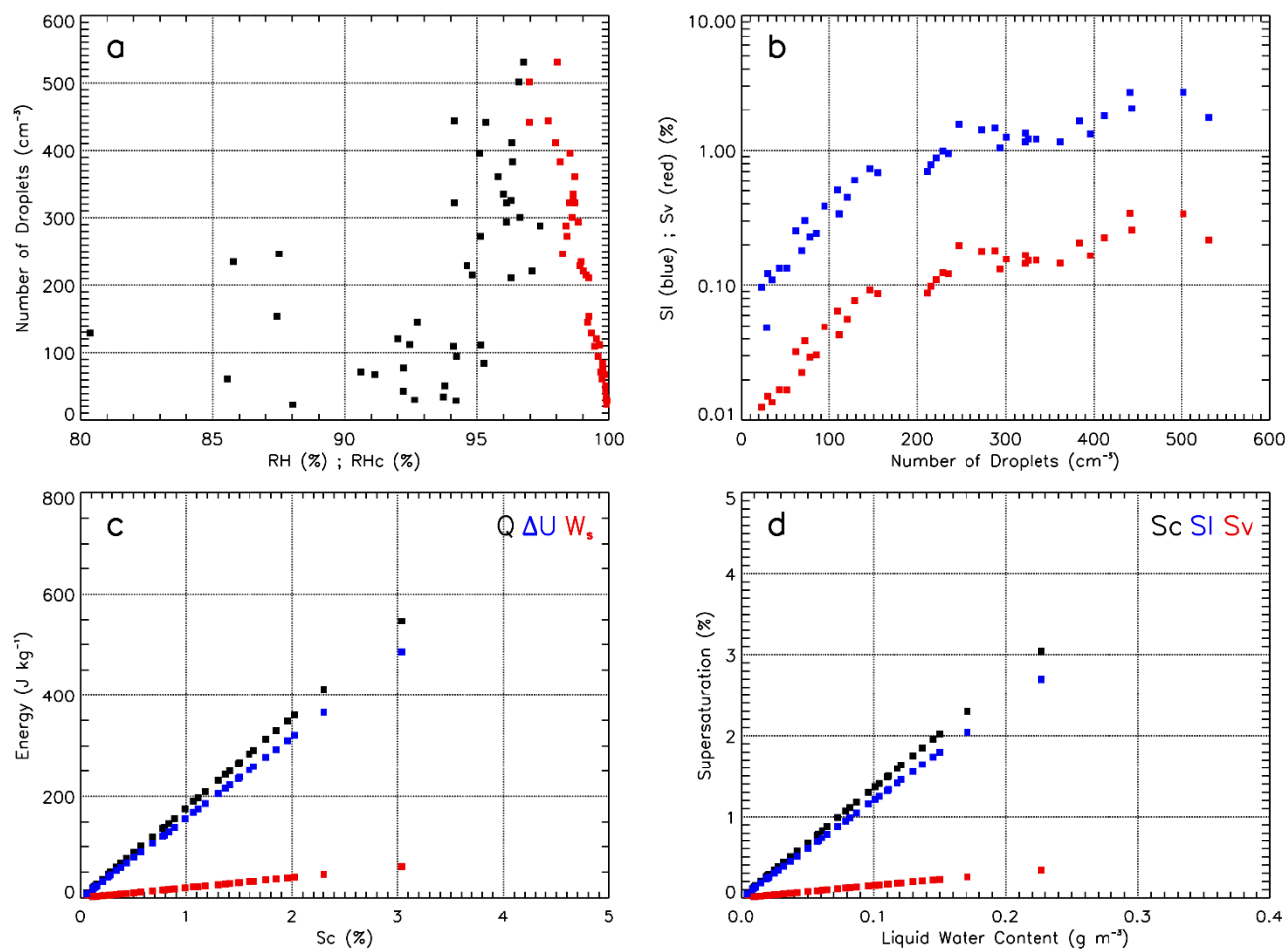


Figure S2. Cloud microphysical and thermodynamic properties measured at cloud bases of growing convective cumuli during Flight AC14. (a) RH versus N_d (black) and RH_c versus N_d (red). Values shown for RH_c do not account for the additional S_v . (b) N_d versus S_i (blue) and N_d versus S_v (red). (c) S_c versus Q , $|\Delta U_{ws}|$ (indicated as ΔU for simplicity), and W_s .

40 (d) LWC versus S_c , S_i , and S_v .

Flight AC09: Northern Amazon



45 Figure S3. Similar to Figure S2 for flight segment AC09.

Flight AC11: Central Amazon

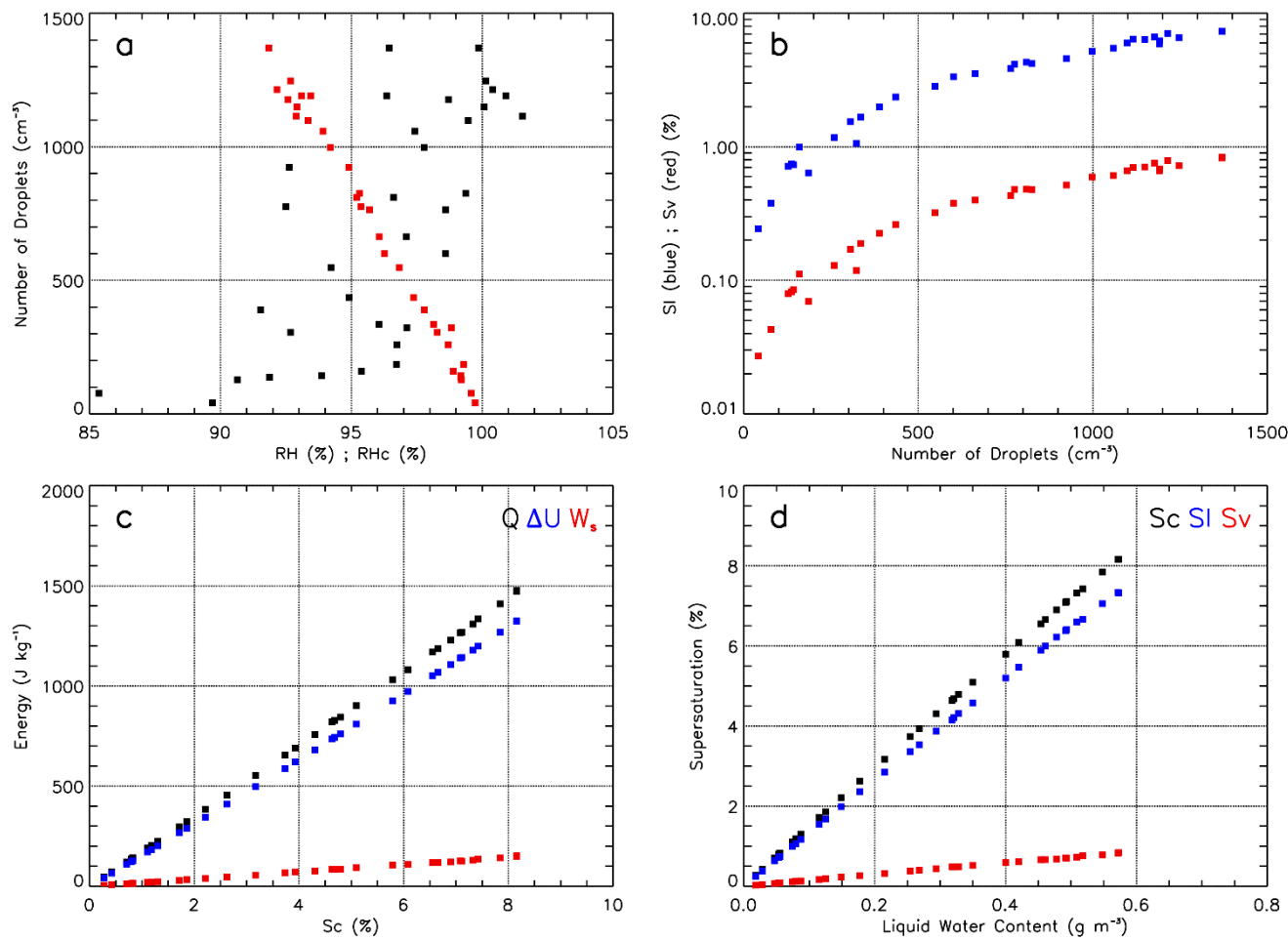


Figure S4. Similar to Figure S2 for flight segment AC11.

Flight AC17a: Central Amazon

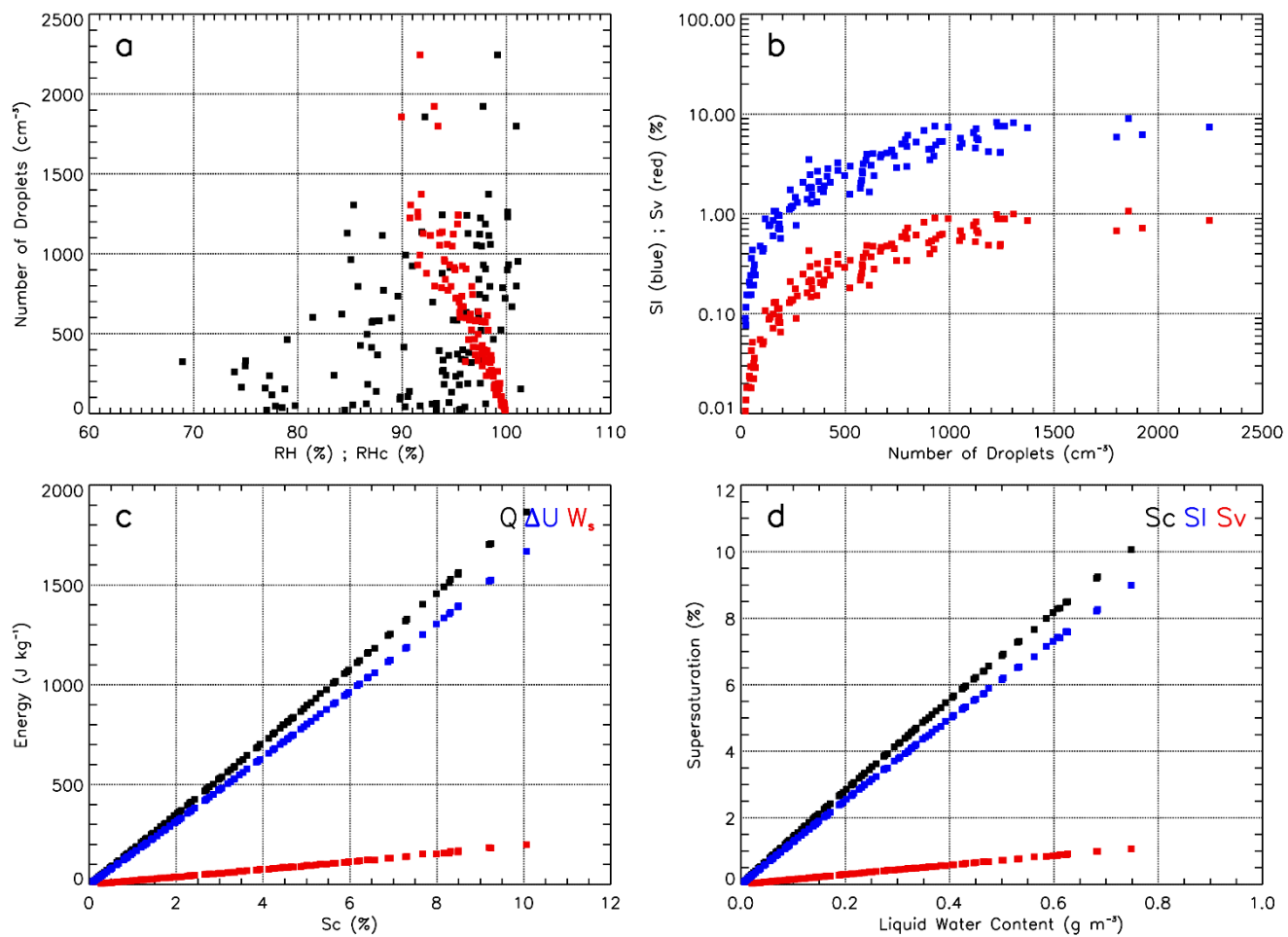


Figure S5. Similar to Figure S2 for flight segment AC17a.

Flight AC17b: Central Amazon

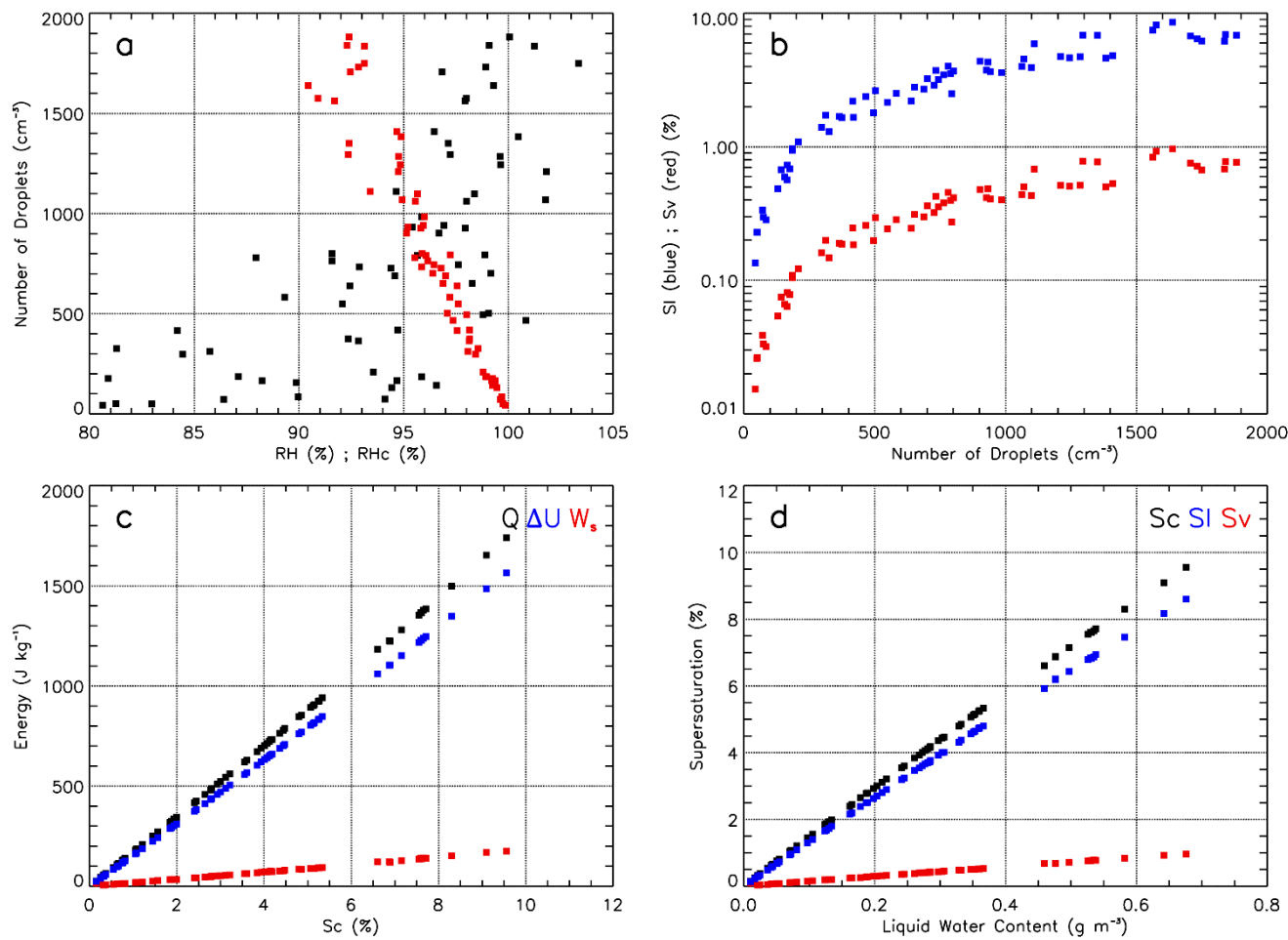


Figure S6. Similar to Figure S2 for flight segment AC17b.

Flight AC18: Northern Amazon

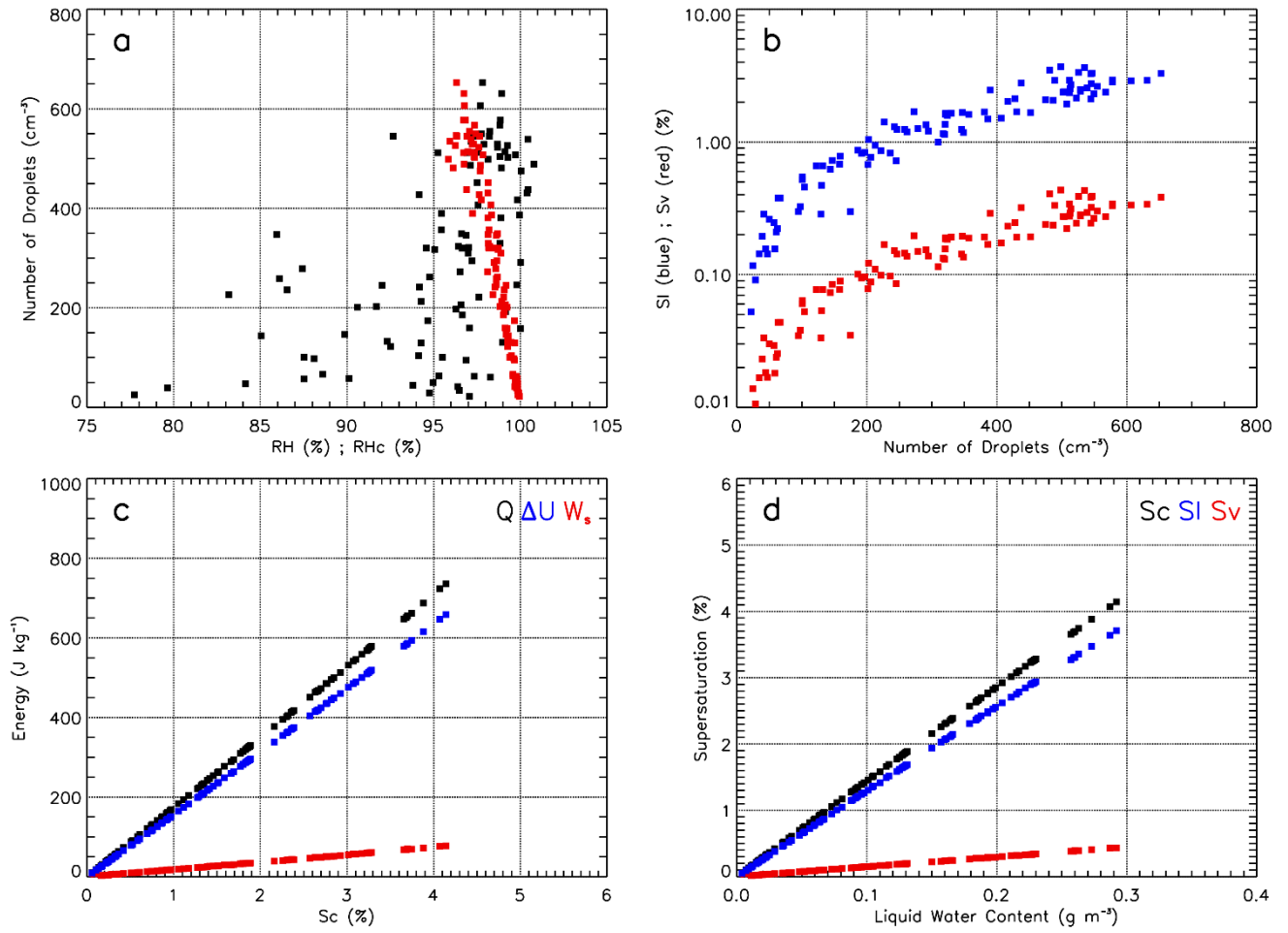


Figure S7. Similar to Figure S2 for flight segment AC18.

Flight AC19: Atlantic Ocean

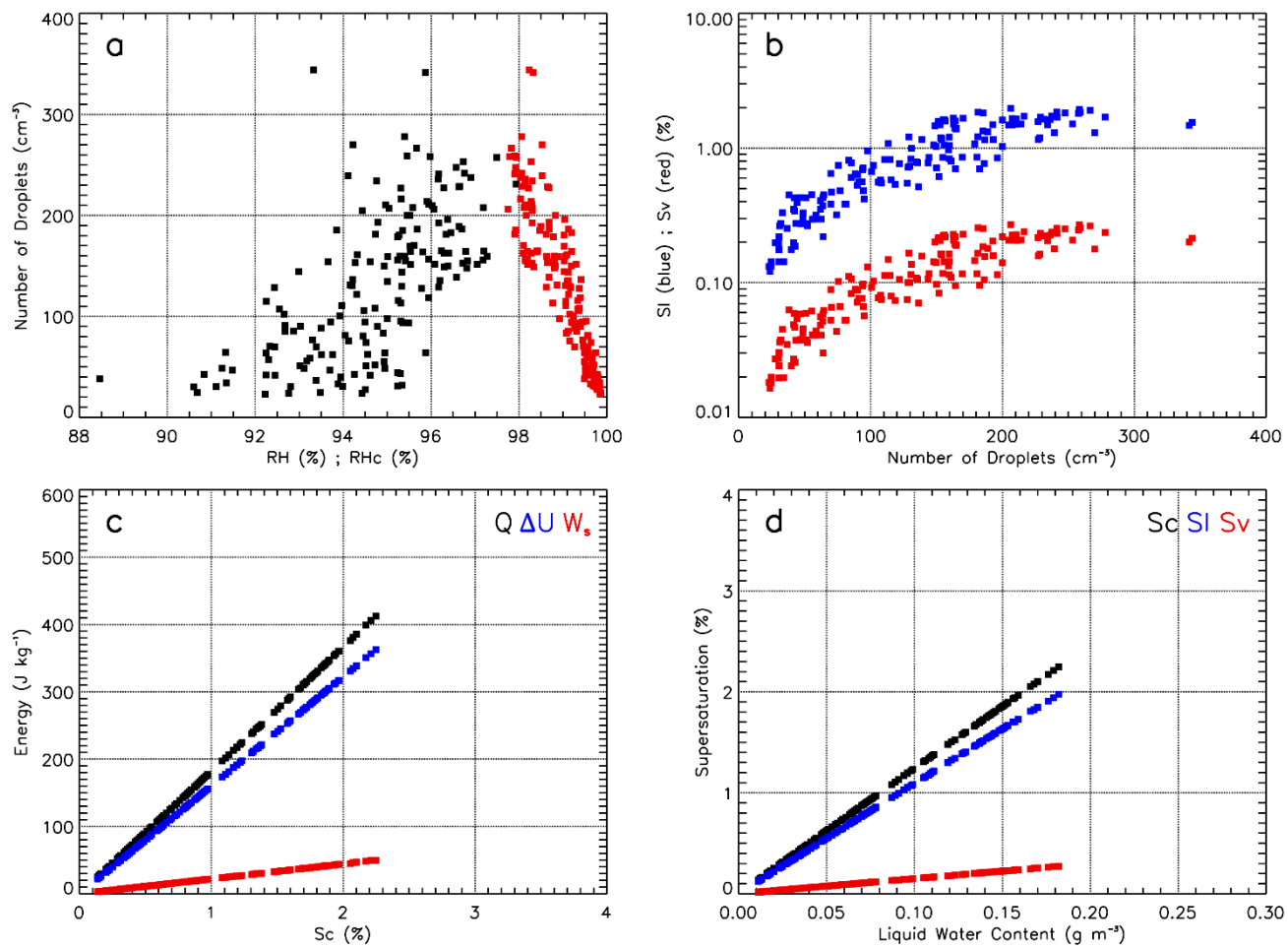


Figure S8. Similar to Figure S2 for flight segment AC19.

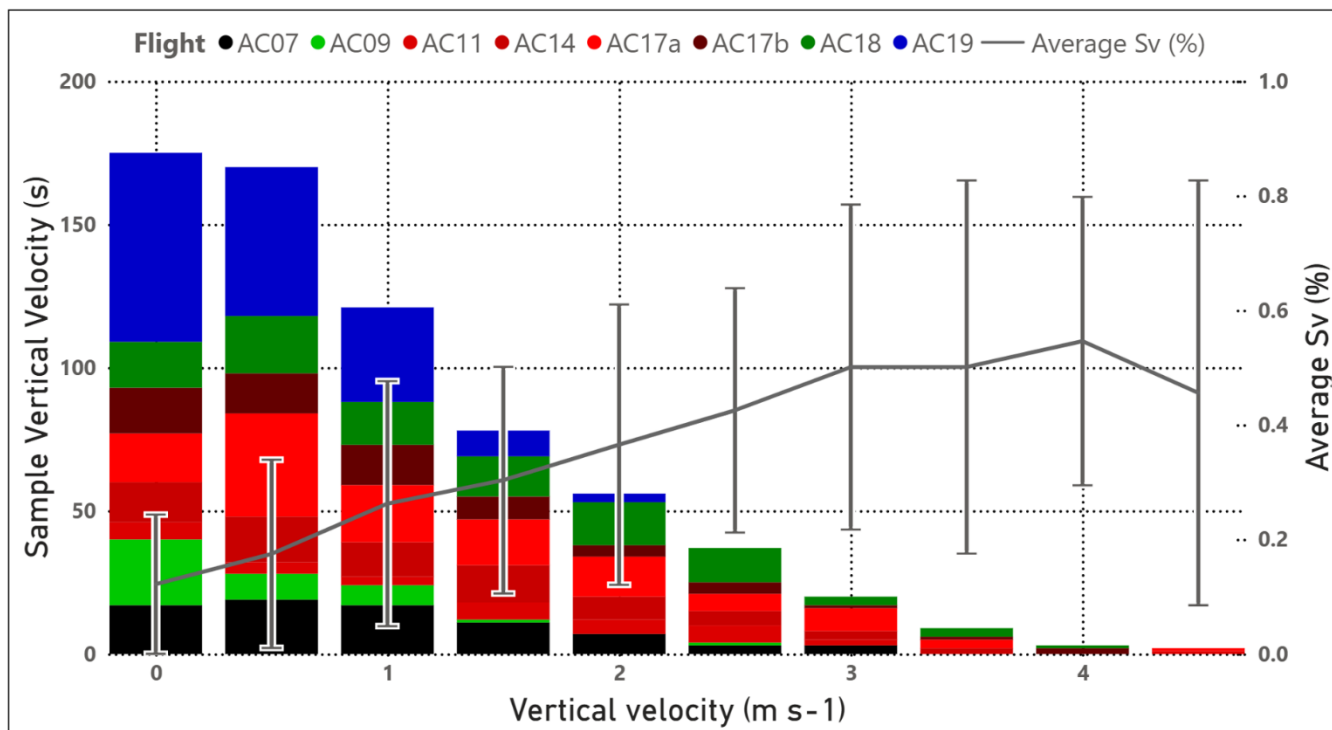
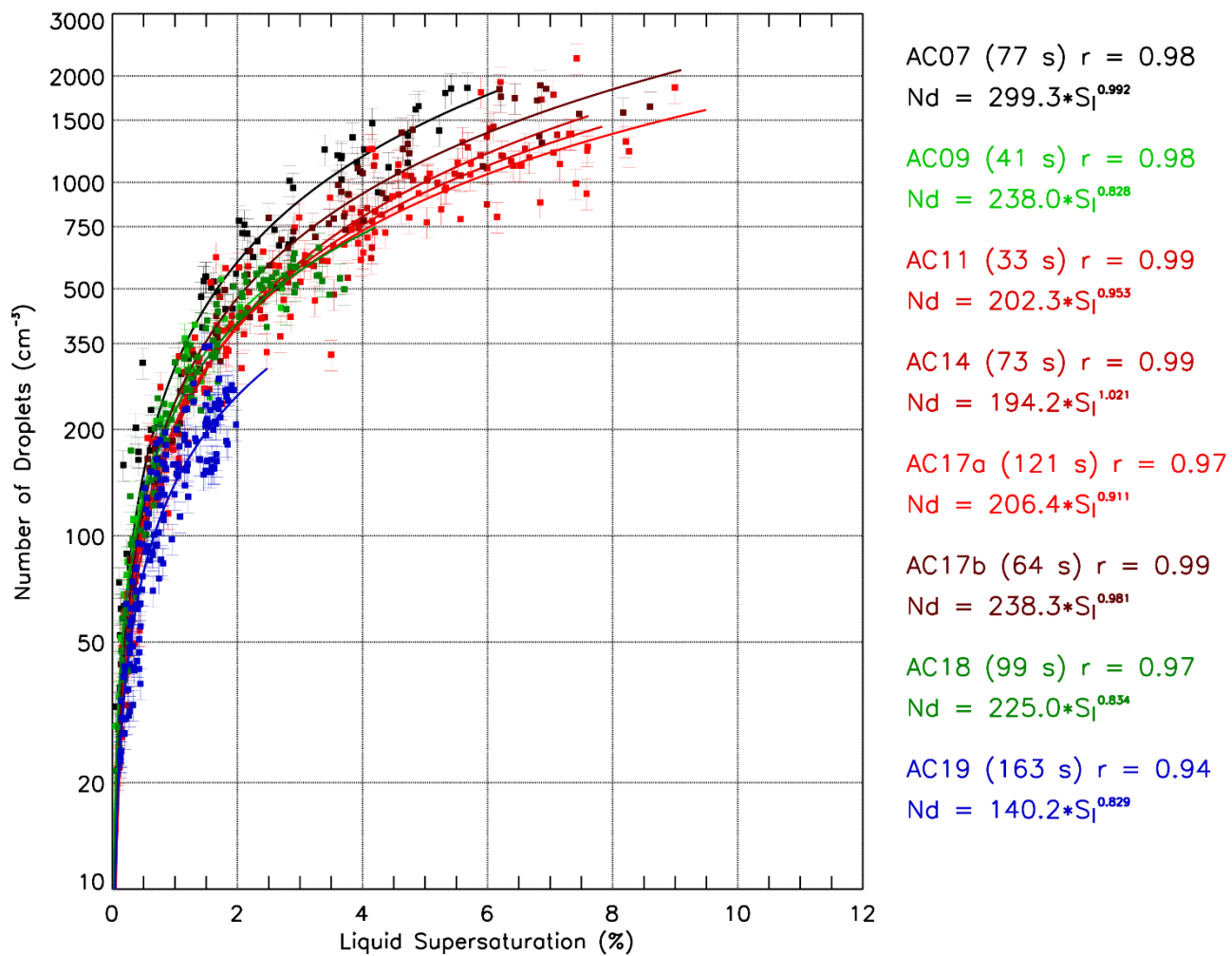


Figure S9. Vertical velocities at cloud base, binned in 0.5 m s^{-1} intervals, shown as the sample time of measurements (left y-axis). The solid line and error bars indicate the average water vapor supersaturation (Sv) and its standard deviations (right y-axis). Colors represent the different flight segments, as indicated in the legend.



100 Figure S10. Similar to Figure 4 for $N_d(S_l)$ spectra measured over the Amazon Basin.

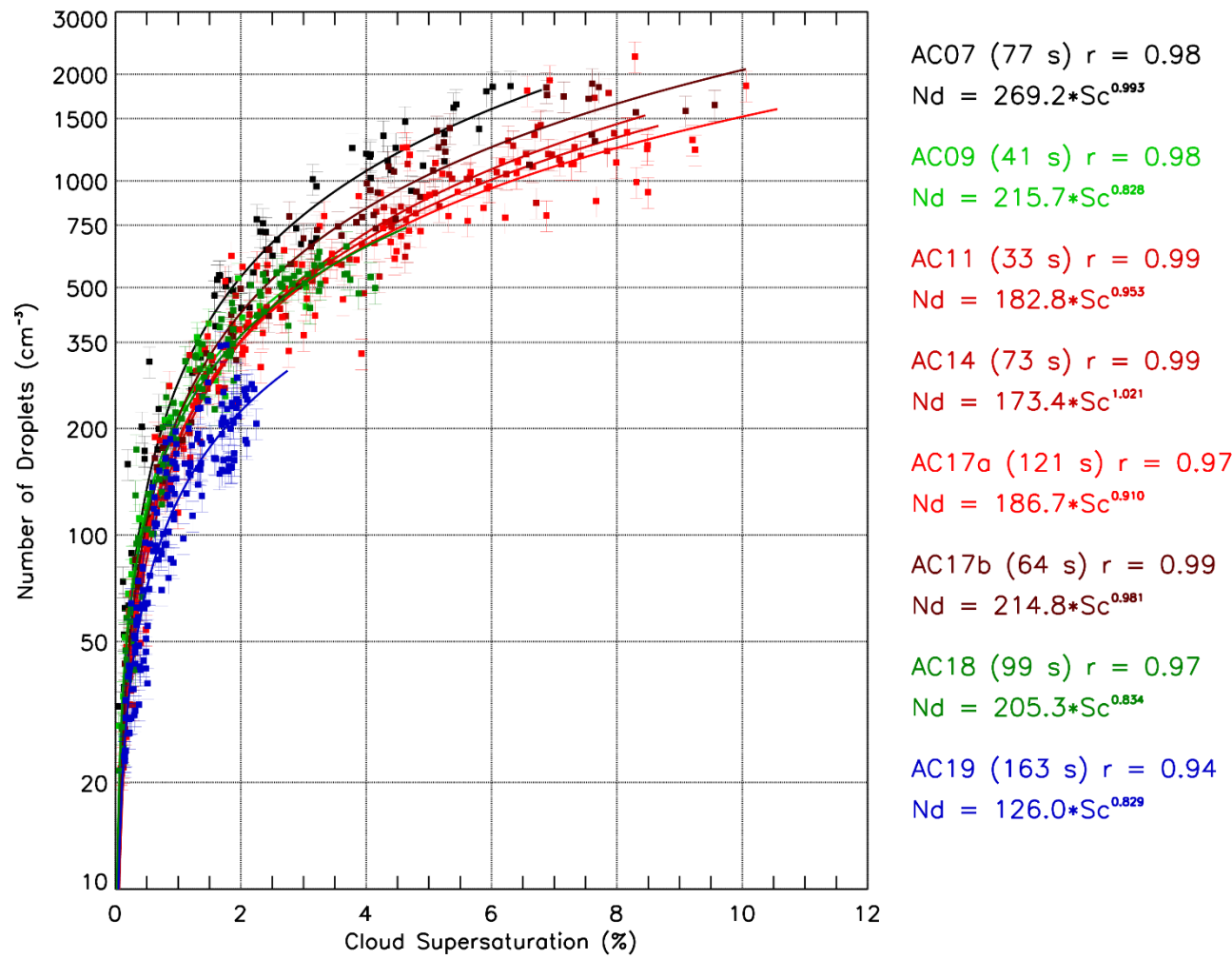


Figure S11. Similar to Figure 4 for $N_d(S_c)$ spectra measured over the Amazon Basin.

S1. Thermodynamic Analysis of the Energetic Budget and Supersaturation at Warm Cloud Base

To illustrate the thermodynamic basis of the energetic budget analysis at cloud base, we first examine the fundamental relationships between air parcel temperature (T), saturation water vapor pressure (e_s), water vapor density (ρ_v), and specific volume of water vapor (α_v), and how these govern RH_c and S_c during the ascent of a saturated parcel in which the condensation of water vapor onto aerosol particles is neglected. These diagnostics provide the basis for associating the energy balance of saturated parcels with the onset of cloud droplet formation at cloud base. Figure S12 presents the theoretical calculations of e_s , ρ_v , α_v , RH_c , and S_c for temperatures between 0°C and 30°C, highlighting the transition from equilibrium saturation ($RH_c = 100\%$, $S_c = 0\%$) at cloud base to supersaturated conditions immediately above cloud base, where the latent heat release from condensational growth of CCN particles and droplets influence the parcel energetics.

Figure S12a shows the relationship between T , e_s , ρ_v and α_v . Both e_s and ρ_v increase exponentially with T and are governed by the Clausius–Clapeyron relation, which defines the threshold that ambient water vapor pressure or vapor density must reach for equilibrium between vapor and liquid. The red line shows α_v , which represents the volume occupied by one gram of water vapor. Unlike ρ_v , α_v decreases rapidly with temperature, reflecting the reduced expansivity of water vapor at higher saturation pressures. These thermodynamic variables describe the conditions leading to air parcel saturation, where at warmer temperatures, a larger amount of water vapor must condense onto CCN particles for activation into cloud droplets at relative humidity $RH = 100\%$.

Figures S12b–c show the values of RH_c and S_c of a saturated air parcel as a function of initial temperature (T_0) and cooling (ΔT) resulting from the adiabatic expansion. At cloud bases ($T = T_0$; $RH_c = 100\%$), the parcel is saturated with respect to water vapor and has no condensed water, and the corresponding supersaturation $S_c = 0\%$. Immediately above cloud base, the ascending saturated parcel experiences cooling, leading to a decrease in e_s . During this process, RH_c is below unity (or 100%) due to the lower internal energy, with corresponding $S_c > 0\%$. For warmer temperatures, the increase in S_c due to adiabatic cooling is relatively low, since e_s reduction relative to the initial e_s is slightly smaller.

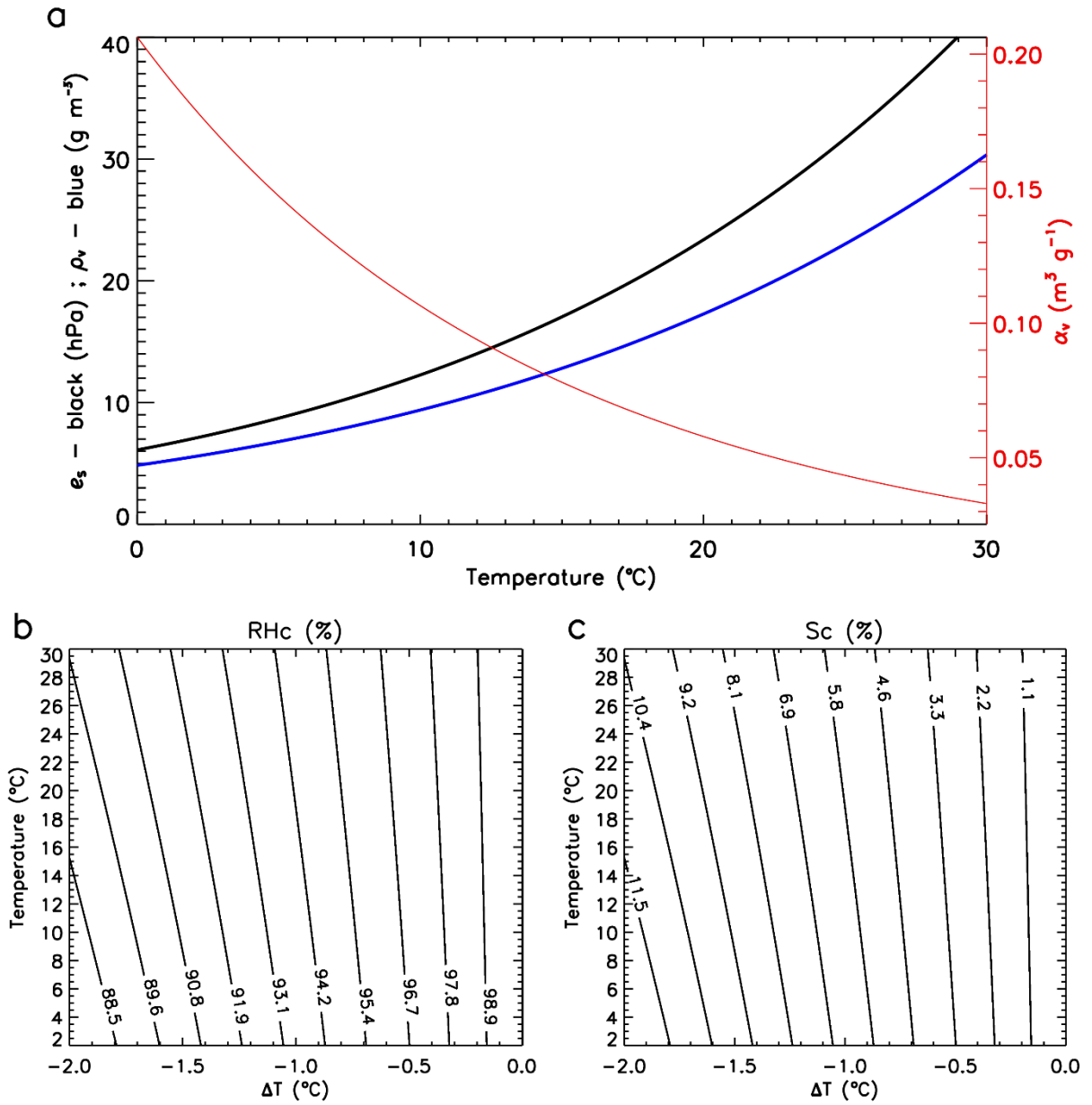


Figure S12. (a) Relationships between air temperature (T), saturation vapor pressure (e_s ; black), water vapor density (ρ_v ; blue), and the specific volume of water vapor (α_v ; red). (b) Relative Humidity of cloud (RH_c) and (c) Cloud supersaturation (S_c) as a function of cloud base initial temperature T_0 [y-axis] and adiabatic cooling rate (ΔT) during expansion [x-axis].

Figure S13 shows the simulated LWC , Q , $|\Delta U_{ws}|$ (indicated as ΔU for simplicity), and W_s resulting from the energy balance for the saturated air parcel, for the temperatures and adiabatic cooling range shown in Figure S12b-c. All quantities from the energy balance are expressed as positive values to represent the partition of the energy from Q into internal energy change and saturation work during the condensational growth. The values were calculated for saturated parcels at a pressure level of 950 hPa. The figure shows that LWC increases approximately linearly with adiabatic cooling. For the same cooling rate, a slightly larger LWC is calculated for lower temperatures owing to the higher dry air density. Since Q is proportional to LWC , its values increase almost linearly with cooling rate for different T_0 , with slightly higher values for warmer T_0 due to the higher e_s . The values of ΔU are slightly smaller than Q since the total energy is partitioned with W_s , and the saturated parcel is slightly warmer than the resulting temperature after adiabatic cooling (see Figure S14). W_s is associated with the cloud entropy of the saturated parcel, which increases approximately linearly with temperature and logarithmically with the cooling rate. For parcels ascending in warmer temperatures, the effective warming is higher since W_s is proportional to T .

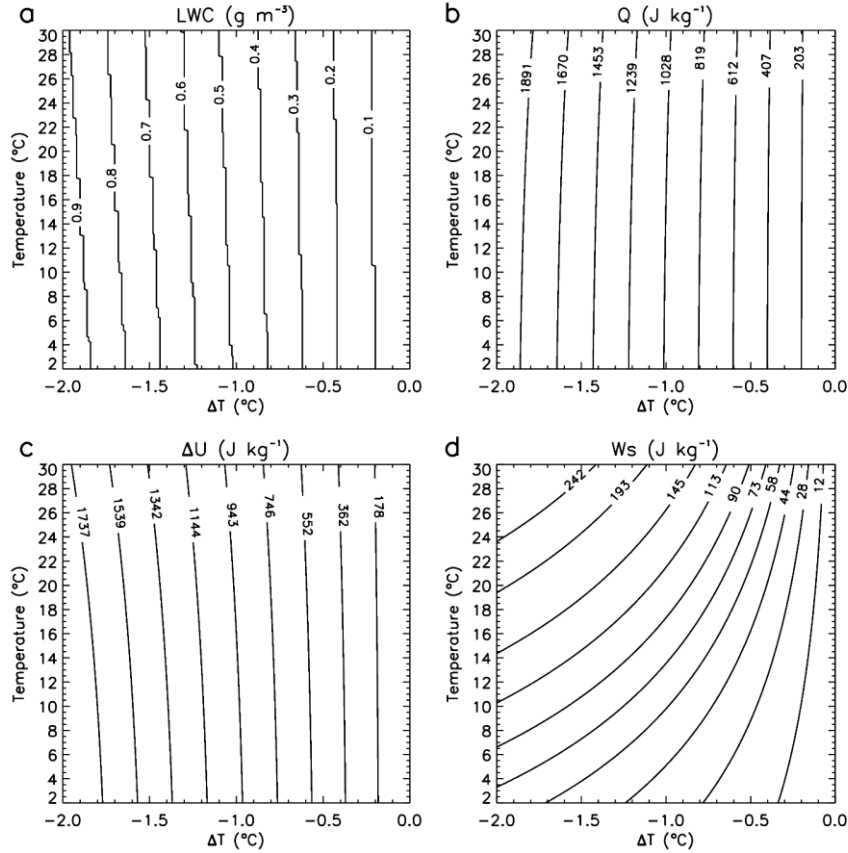


Figure S13. Contours of Liquid Water Content (LWC) values and Energy balance terms of cloud adiabatic parcels as a function of initial temperature T_0 (y-axis) and adiabatic cooling rate (x-axis) at 950 hPa. (a) LWC , (b) Latent heat of condensation (Q), (c) Magnitude of internal-energy change ($|\Delta U|$), and (d) saturation work (W_s).

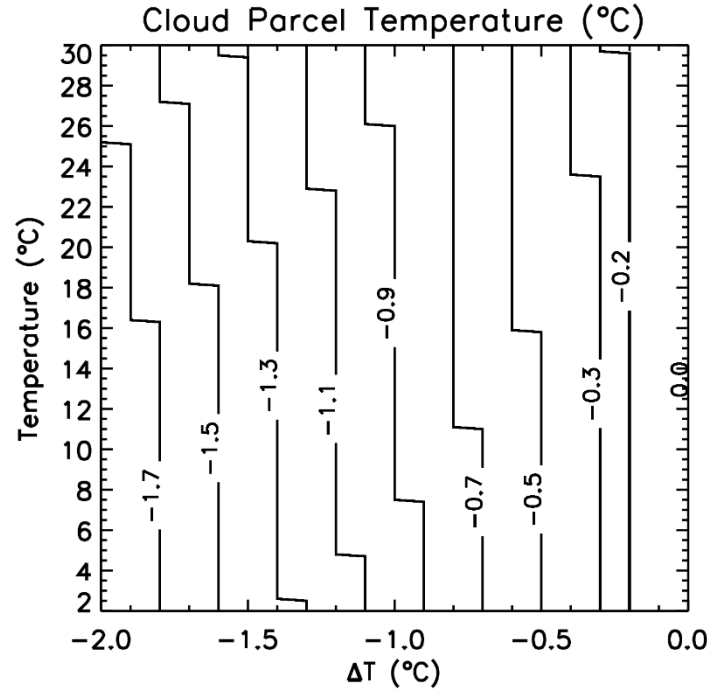


Fig. S14. Temperature of the saturated parcels (contour lines) as a function of initial temperature (T_0) and adiabatic cooling rate (ΔT) resulting from the latent heat released during the condensational growth of cloud particles at 950 hPa. Contours illustrate the effect of W_s in the resulting temperature, which is slightly warmer than ΔT .

Figure S15 presents the partitioning of cloud supersaturation (S_c , shown in Figure S12c) into its liquid-phase (S_l) and vapor-phase (S_v) components for saturated parcels undergoing cooling illustrated in Figure S13. The values of S_l and S_v result from the energy associated with ΔU and W_s , respectively. The figure shows that S_c is dominated by liquid-phase processes, with vapor expansion acting as a smaller fraction of the energetic closure. Since the fraction of energy associated with W_s (FW_s) is larger at warmer temperatures, S_v is relatively higher for the same adiabatic cooling during expansion, whereas the opposite is observed for S_l .

For simulations of warm saturated parcels with similar adiabatic cooling rates and T_0 but at lower pressures than 950 hPa, LWC is lower due to lower air density (see Figure S16 for the case at 800 hPa). However, a similar Q is calculated since it depends weakly on atmospheric pressure. The values of Q , ΔU , and W_s remain with similar proportions, where most of the energy resulting from the condensational growth is converted to a decrease in the internal energy of the saturated parcel.

170 Slightly higher W_s were simulated at lower pressure (800 hPa) due to the higher saturation mixing ratio in this case (see Eqs. 8 and 21). Thus, slight changes in S_l and S_v values were simulated (see Figure S20).

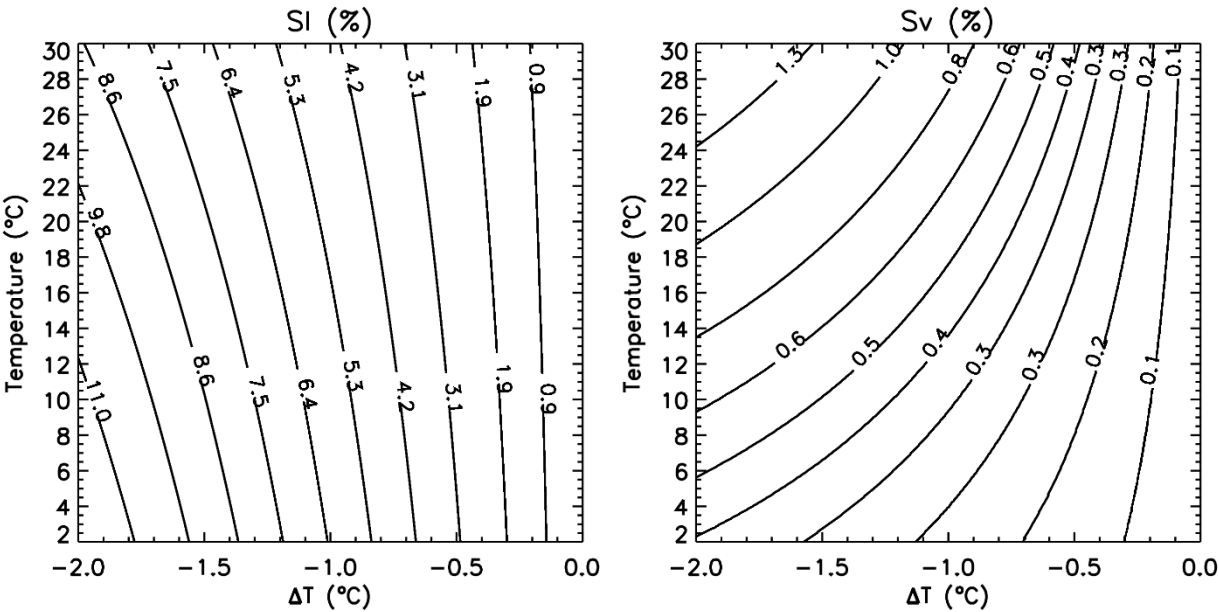


Figure S15. [left] Contours of liquid-phase supersaturation (S_l) values for saturated parcels at 950 hPa, shown as a function of initial cloud base temperature T_0 and adiabatic cooling rate (ΔT). [right] similar for water vapor supersaturation (S_v).

175

180

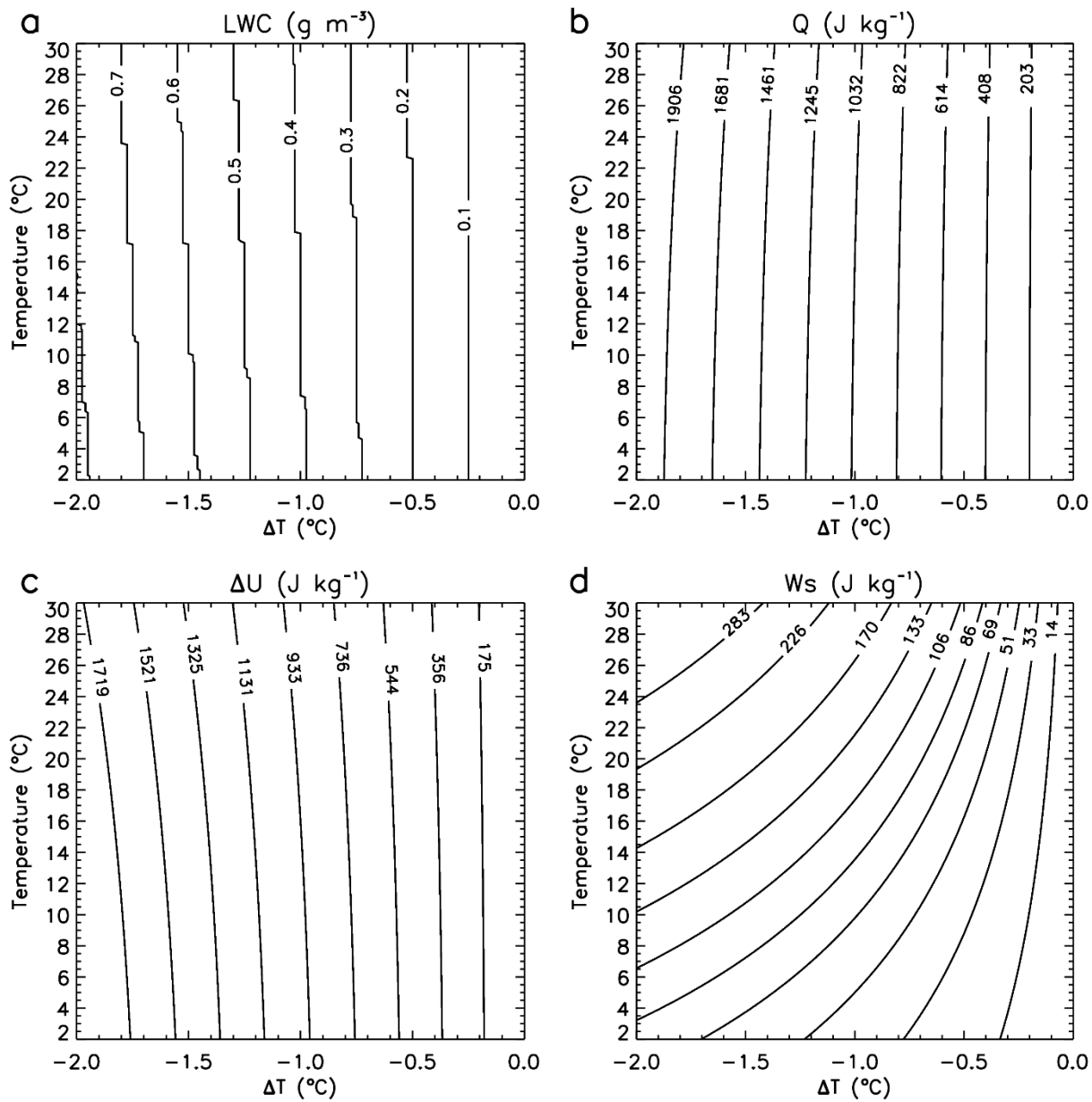


Fig.

Figure S16. Similar to Figure S13 at 800 hPa.

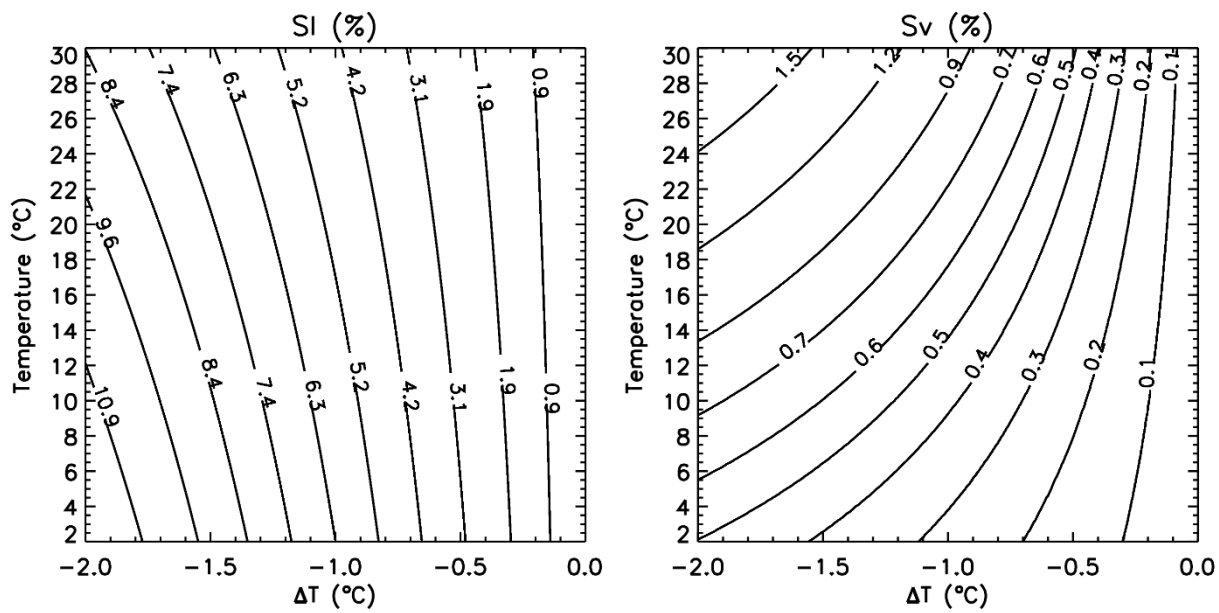


Figure S17. Similar to Figure S15 at 800 hPa.